Supporting information for

Ultra-High Power Efficiency Organic Light-Emitting Diodes Based on Hot-Exciton-Assisted Exciplex (HEAE) System

Jingli Lou, Junwei He, Baoxi Li, Han Zhang*,Yichao Chen, Ben Zhong Tang, Zhiming Wang*

General information

All chemicals and reagents were purchased from commercial sources and used as received. The final product underwent vacuum sublimation to improve purity before measuring its PL and EL properties. ^{1}H and ^{13}C NMR spectra were recorded on a Bruker AV 500 spectrometer in CD_2Cl_2 at room temperature. High-resolution mass spectroscopy was performed on a GCT premier CAB048 mass spectrometer operating in MALDITOF mode.

Computational methods

All density functional theory (DFT) calculations were performed using the Gaussian 16 package. The optimized S_0 geometry and single-point properties at S_0 were calculated using the DFT method at the M06-2X/6-31G (d,p) level. The S_1 geometry was optimized using time-dependent DFT (TD-DFT) at the M06-2X/6-31G (d,p) level. NTO and energy levels of the first five S_1 and T_1 states were calculated based on the S_1 geometry at the M06-2X/6-31G(d,p) level to understand the excited-state properties.

***Gibbs* free energy of exciplex formation**

The driving force for the formation of exciplex in the state of mixing film can be estimated by calculating the *Gibbs* free energy (ΔG) of exciplex components, as the following formula shown:

$$-\Delta G = E_{ox,D} - E_{red,A} - constant$$

where $E_{ox,D}$ is the oxidation potential of donor, $E_{red,A}$ is the reduction potential of acceptor, and the value of the constant is between 0~0.20 eV. It was found that the ΔG values of the exciplexes H1, H2, and H3 were 2.05, 1.01, and 1.83 eV, respectively, indicating the 2MCz-CNMCz, 2*t*-2MCz-CNMCz, and 4*t*-2MCz-CNMCz were well matched with PO-T2T.

Photophysical property measurements

Solutions with a concentration of 1×10^{-5} M were prepared for the solution measurements. All organic films used for the PL measurements were deposited onto clean quartz substrates via thermal evaporation at 1–1.5 Å s^{-1} under high vacuum with a base pressure of $< 10^{-5}$ torr. Ultraviolet–visible (UV–vis) absorption spectra were measured on a Shimadzu UV-2600 spectrophotometer. PL spectra were recorded on a Horiba Fluoromax-4 spectrofluorometer. PLQYs were measured using a Hamamatsu absolute PL quantum yield spectrometer (C11347 Quantaurus_QY). Transient PL decay curves were measured using an Edinburgh Instrument FLS1000 spectrometer.

Electrochemical and thermal stability measurements

Cyclic voltammetry was conducted on a CHI 610E A14297 using a solution of tetra-*n*-butylammonium hexafluorophosphate (Bu_4NPF_6) (0.1 M) in dichloromethane or dimethylformamide at a scan rate of 100 mV s^{-1}. A platinum wire was used as the auxiliary

electrode, a glass carbon disk as the working electrode, and Ag/Ag^+ as the reference electrode, with the redox couple ferricenium/ferrocene (Fc/Fc^+) serving as the calibration standard. The ionization potential (IP_{CV}) and electron affinities (EA_{CV}) of these molecules were calculated using the following formulas: $IP_{CV} = (E_{ox} - E_{1/2}(Fc/Fc^+) + 4.8)$ eV and $EA_{CV} = (E_{red} - E_{1/2}(Fc/Fc^+) + 4.8)$ eV, where E_{ox} and E_{red} represent the onset oxidation potential and reduction potential relative to Fc/Fc^+ (4.8 eV), respectively. Thermogravimetric analysis was performed on a Netzsch TG 209 under nitrogen flow at a heating rate of 10°C min^{-1}. Differential scanning calorimetric (DSC) was performed on a Netzsch DSC 200 F3 under nitrogen flow at a heating rate of 10°C min^{-1}.

OLED fabrication and characterization

The glass substrates, precoated with a 90 nm layer of ITO with a sheet resistance of 15 to 20 ohms per square, were successively cleaned in ultrasonic bath of acetone, isopropanol, detergent, and deionized water, respectively, with each step lasting 10 min. Then, the substrates were completely dried in a 70°C oven. To improve the hole injection ability of ITO, the substrates underwent O_2 plasma treatment for 6 min before fabrication. The vacuum-deposited OLEDs were fabricated under a pressure of $< 5 \times 10^{-4}$ Pa in the Suzhou Fangsheng FS-380 vacuum deposition system. Organic materials, LiF, and Al were deposited at rates of 0.5 to 1.5 A, 0.1, and 3 A s^{-1}, respectively. The effective emitting area of the device was 9 mm^2, determined by the overlap between the anode and cathode. EL spectra, luminance–voltage–current density, and EQE were characterized with a dual-channel Keithley 2400 source meter and a PR-670 spectrometer. All characterizations were conducted at room temperature and in ambient conditions without encapsulation, immediately after fabrication.

Transient Absorption Proofs of *h*RISC

The ultrafast photophysical dynamics of 2MCz-CNMCz in toluene solution were monitored using femtosecond and nanosecond transient absorption (fs/ns-TA) spectroscopy with 350 nm excitation (pulse energy: 26 μW) (Figure S1). Within the initial 0.3−60.8 ps (Figure S1a top), the TA spectra exhibited a distinct negative signal in the 380–440 nm regions, attributed to stimulated emission (SE, $S_1 \rightarrow S_0$ emission), respectively. Positive signals observed between 550–700 nm was assigned to excited-state absorption (ESA, $S_1 \rightarrow S_n$). Notably, both the SE band around 380–440 nm and the ESA signal spanning 550–700 nm exhibited pronounced bathochromic shifts. The signal evolutions could be attributed to the conformational relaxation of the S_1, which involves vibrationally relaxing from higher to lower vibrational modes. The stationary SE band was consistent with the steady-state PL spectrum of 2MCz-CNMCz in toluene solution. Between 60.8 ps and 4.7 ns, the decay of SE signals fully coincided with the

decay of ESA signals ranging from 550 to 700 nm, further indicating that these TA signals originated from the S_1 state. To investigate spectral evolution in detail, a global kinetic-fitting analysis was performed. The fs-TA kinetics of 2MCz-CNMCz at 393 nm were monitored (Figure S1b), yielding three decay lifetimes of τ_{grow1} = 0.14 ps, τ_{grow2} = 7.22 ps, τ_{decay1} = 263.67 ps, and τ_{decay2} = 0.85 ns. The τ_{grow1} and τ_{grow2} lifetime corresponded to higher-frequency vibration and conformational relaxation. The τ_{decay2} was assigned to the fluorescence lifetime, which closely aligned with the time-resolved decay results (1.00 ns). Based on the reported model, the τ_{decay1} could be attributed to the lifetime of the dynamic equilibrium on the interconversion process of ISC and RISC.[1]

As triplet state evolution is not fully captured in fs-TA spectroscopy, nanosecond transient absorption (ns-TA) spectroscopy was performed (Figure S1c). The ESA signal spanning 550–750 nm decayed and was completely weakened from 5.34 ns to 5.94 μs, which was assigned to excited-state absorption ($T_1 \rightarrow T_n$). The SE signal in the 380–440 nm regions decayed until 5.34 ns, interestingly, an increased absorption signal around 416 nm was detected from 5.34 ns to 8.98 ns (grey cycle in Figure S1d), suggesting a possible ultrafast rate constant for the ISC process. The ns-TA decay kinetics at 416 nm were fitted with a multi-exponential function (Figure S1e), revealing three lifetimes of τ_{grow} = 1.05 ns, τ_{decay1} = 12.28 ns, and τ_{decay2} = 1.01 μs. These lifetimes were assigned to intersystem crossing ($S_1 \rightarrow T_n$ transition), internal conversion ($T_n \rightarrow T_1$ transition), and phosphorescence decay ($T_1 \rightarrow S_0$ transition), respectively. Based on fs/ns-TA spectra, the mechanistic diagram of 2MCz-CNMCz exciton was depicted in Figure S1f. Five distinct processes were revealed as 1 for conformational relaxation, 2 for high-lying intersystem crossing (*h*ISC) and *h*RISC, 3 for fluorescence, 4 for internal conversion, and 5 for phosphorescence. According to the TA fitting lifetimes and equations, the rate constants were successfully extracted and summarized in Table S1. Notably, the rate constant of reverse intersystem crossing (k_{hRISC}) was 2.42×10^9 s^{-1}, significantly higher than those of intersystem crossing $k_{hISC} = 1.37 \times 10^9$ s^{-1} and internal conversion $k_{IC} = 0.82 \times 10^8$ s^{-1} for high-lying triplet excitons. These results provided direct mechanistic evidence of the involvement of high-lying triplet states in the intersystem crossing.

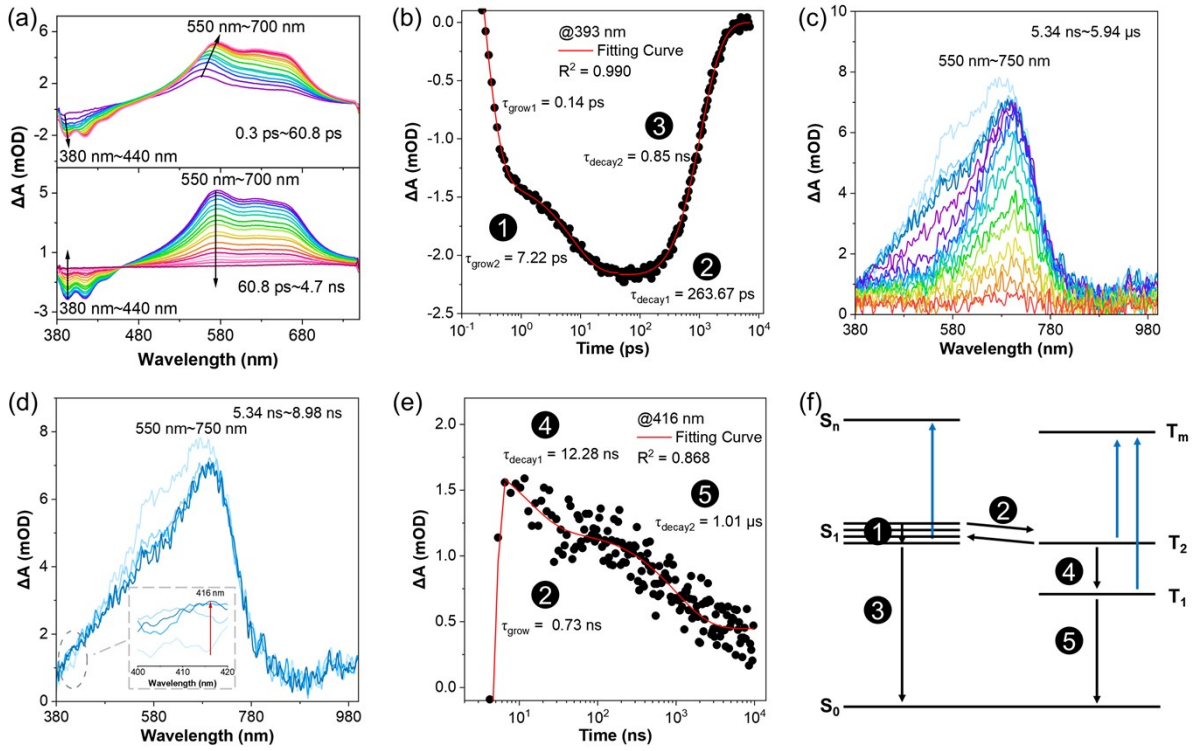

Figure S1. Transient absorption of 2MCz-CNMCz toluene solution measured at room temperature. (a) Femtosecond transient absorption spectra ranging from 0.3 ps to 60.8 ps (top) and from 60.8 ps to 4742 ps (bottom). Time-dependent diagram of (b) difference absorption signals (ΔA) monitoring at 393 nm from 0.3 ps to 7043 ps. (c) Nanosecond transient absorption spectra ranging from 5.34 ns to 5.94 μs. (d) Nanosecond transient absorption spectra ranging from 5.34 ns to 8.98 ns. (e) Time-dependent diagram of difference absorption signals (ΔA) monitoring at 416 nm from 5.34 ns to 9680 ns. (f) Mechanistic diagram of 2MCz-CNMCz (1: conformational relaxation; 2: high-lying intersystem crossing (*h*ISC) and *h*RISC; 3: fluorescence; 4: internal conversion; 5: phosphorescence).

Table S1. Rate constants of 2MCz-CNMCz.

Compound	τ_F /10^{-9} s	τ_{IC} /10^{-9} s	τ_{ISC} /10^{-9} s	$\tau_{equilibration}$ /10^{-9} s	k_r/10^8 s^{-1} (S_1)	k_{IC}/10^8 s^{-1} (T_2)	k_{ISC}/10^8 s^{-1}	k_{RISC}/10^8 s^{-1}	η_r /%
2MCz-CNMCz	0.85	12.18	0.73	0.26	11.76	0.82	13.70	24.18	77.1

$k_r = 1/\tau_F$

$k_{IC} = 1/\tau_{IC}$

$k_{ISC} = 1/\tau_{ISC}$

$k_{ISC} + k_{RISC} = 1/\tau_{equilibration}$

where k_r = fluorescence decay rate constant; k_{IC} = internal conversion rate constant; k_{ISC} = intersystem crossing rate constant from S_1 to T_2 state; k_{RISC} = rate constant of reverse intersystem crossing. τ_F, τ_{IC} and τ_{ISC} are lifetimes of fluorescence decay, internal conversion,

and intersystem crossing, respectively. $\tau_{equilibration}$ is the equilibrium of singlet and triplet excitons. η_r is the exciton utilization efficiency.

Synthesis and characterization:

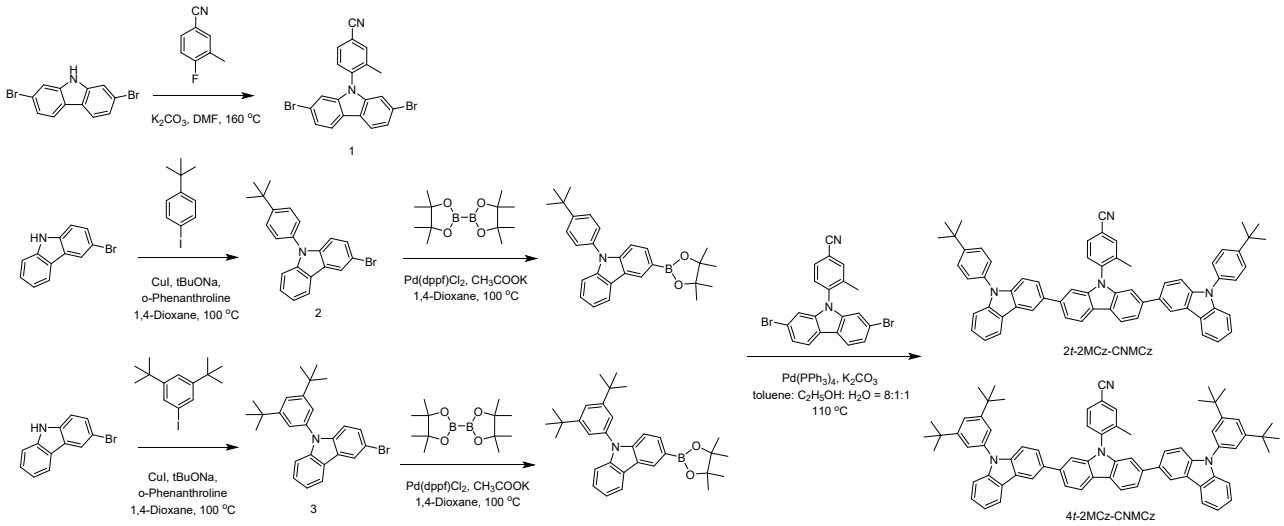

Scheme S1. Molecular structure and synthetic route of 2*t*-2MCz-CNMCz and 4*t*-2MCz-CNMCz.

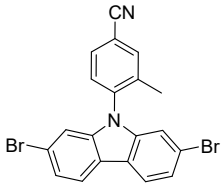

4-(2,7-dibromo-9H-carbazol-9-yl)-3-methylbenzonitrile (**1**): Compound 1 was prepared according to the method reported in the literature.[2]

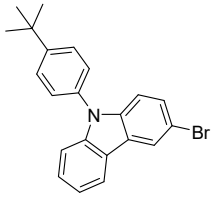

(9-(4-(tert-butyl)phenyl)-9H-carbazol-3-yl)boronic acid (**2**): 3-bromo-9H-carbazole (1.48 g, 6 mmol), 1-(tert-butyl)-4-iodobenzene (1.82 g, 7.2 mmol), acetic acid (2.28 g, 7.2 mmol), and $PdCl_2$(dppf) (0.2g, 0.3 mmol) were placed in a 100 mL round bottom flask and stirred for 30 min under nitrogen at room temperature. Then 50 mL 1,4-dioxane was injected into the bottle, and the reaction mixture refluxed for 12 h under a nitrogen atmosphere. After cooled to room temperature, the reaction mixture was poured into a large amount of water and extracted twice with DCM. evaporated this reaction solution under reduced pressure. After the solvent was evaporated under reduced pressure, the residue was purified by column chromatography on silica-gel (dichloromethane/petroleum) to afford white solid of 1.5 g in 73% yield. ^{1}H NMR

(500 MHz, CD_2Cl_2) δ 8.26 (d, *J* = 2.0 Hz, 1H), 8.10 (d, *J* = 7.8 Hz, 1H), 7.63 (d, *J* = 8.6 Hz, 2H), 7.50 – 7.44 (m, 3H), 7.44 – 7.39 (m, 2H), 7.32 – 7.26 (m, 2H), 1.42 (s, 9H).

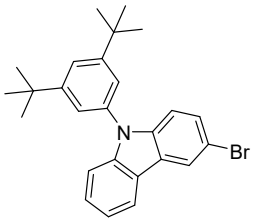

3-bromo-9-(3,5-di-tert-butylphenyl)-9H-carbazole (**3**): 3-bromo-9H-carbazole (1.48 g, 6 mmol), 1,3-di-tert-butyl-5-iodobenzene (2.28 g, 7.2 mmol), acetic acid (2.28 g, 7.2 mmol), and $PdCl_2$(dppf) (0.2g, 0.3 mmol) were placed in a 100 mL round bottom flask and stirred for 30 min under nitrogen at room temperature. Then 50 mL 1,4-dioxane was injected into the bottle, and the reaction mixture refluxed for 12 h under a nitrogen atmosphere. After cooled to room temperature, the reaction mixture was poured into a large amount of water and extracted twice with DCM. evaporated this reaction solution under reduced pressure. After the solvent was evaporated under reduced pressure, the residue was purified by column chromatography on silica-gel (dichloromethane/petroleum) to afford white solid of 1.7 g in 65% yield. ^{1}H NMR (400 MHz, CD_2Cl_2) δ 8.27 (s, 1H), 8.10 (d, *J* = 7.8 Hz, 1H), 7.54 (d, *J* = 6.7 Hz, 1H), 7.50 (d, *J* = 8.7 Hz, 1H), 7.47 – 7.41 (m, 2H), 7.37 (s, 2H), 7.30 (dd, *J* = 11.7, 6.2 Hz, 2H), 1.39 (s, 18H).

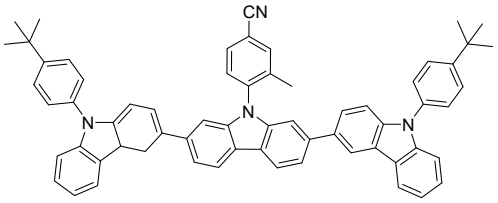

4-(9,9''-bis(4-(*tert*-butyl)phenyl)-9*H*,9'*H*,9''*H*-[3,2':7',3''-tercarbazol]-9'-yl)-3-methylbenzonitrile (**2*t*-2MCz-CNMCz**): A mixture of compound 4-(2,7-dibromo-9H-carbazol-9-yl)-3-methylbenzonitrile (0.44 g, 1 mmol), (9-(4-(tert-butyl)phenyl)-9H-carbazol-3-yl)boronic acid (1.03 g, 3 mmol), Pd(PPh3)4 (0.12 g, 0.1 mmol) and K_2CO_3 (0.48 g, 3.5 mmol) was added in 250 mL two-neck bottle under nitrogen. Then, a mixed solvent system of toluene, C_2H_5OH and H_2O (v/v/v = 8:1:1) was injected into the bottle, and the reaction mixture was refluxed for 7 h. After cooling to room temperature, the mixture was poured into water and extracted twice with dichloromethane, and then dried over anhydrous magnesium sulfate. After filtration, the solvent was evaporated under reduced pressure and the residue was purified by silica-gel column chromatography (dichloromethane/petroleum). White solid of 2*t*-2MCz-CNMCz was obtained 0.48 g in 55% yield. ^{1}H NMR (400 MHz, CD_2Cl_2) δ 8.40 (s, 2H), 8.28 (d, *J* = 8.0 Hz, 2H), 8.21 (d, *J* = 7.7 Hz, 2H), 7.89 (s, 1H), 7.81 (d, *J* = 8.1 Hz, 1H), 7.75 – 7.63

(m, 9H), 7.54 – 7.41 (m, 10H), 7.37 – 7.28 (m, 4H), 2.19 (s, 3H), 1.44 (s, 18H). ^{13}C NMR (101 MHz, CD_2Cl_2) δ 151.11, 140.87, 136.11, 131.87, 130.98, 127.27, 126.75, 126.55, 126.08, 124.17, 123.67, 122.36, 121.12, 120.64, 120.35, 119.28, 118.85, 113.08, 110.53, 108.32, 35.12, 31.56, 18.11. HRMS: *m/z* calculated for $C_{64}H_{52}N_4Na^+$: 899.4084 [*M*+Na]$^+$, found: 899.4086.

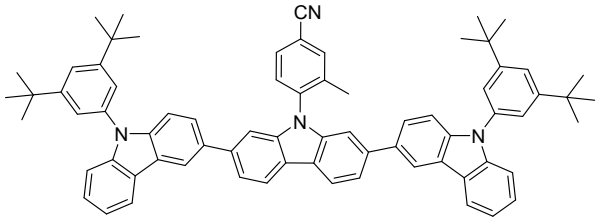

4-(9,9"-bis(3,5-di-*tert*-butylphenyl)-9*H*,9'*H*,9"*H*-[3,2':7',3"-tercarbazol]-9'-yl)-3-methylbenzonitrile (**4*t*-2MCz-CNMCz**): A mixture of compound 4-(2,7-dibromo-9H-carbazol-9-yl)-3-methylbenzonitrile (0.44 g, 1 mmol), (9-(3,5-di-tert-butylphenyl)-9H-carbazol-3-yl)boronic acid (1.20 g, 3 mmol), $Pd(PPh_3)_4$ (0.12 g, 0.1 mmol) and K_2CO_3 (0.48 g, 3.5 mmol) was added in 250 mL two-neck bottle under nitrogen. Then, a mixed solvent system of toluene, C_2H_5OH and H_2O (v/v/v = 8:1:1) was injected into the bottle, and the reaction mixture was refluxed for 7 h. After cooling to room temperature, the mixture was poured into water and extracted twice with dichloromethane, and then dried over anhydrous magnesium sulfate. After filtration, the solvent was evaporated under reduced pressure and the residue was purified by silica-gel column chromatography (dichloromethane/petroleum). White solid of 4*t*-2MCz-CNMCz was obtained 0.49 g in 50% yield. ^{1}H NMR (400 MHz, DMSO) δ 8.63 (d, *J* = 1.2 Hz, 2H), 8.41 (dd, *J* = 10.7, 8.0 Hz, 4H), 8.19 (s, 1H), 8.05 – 8.01 (m, 1H), 7.87 – 7.78 (m, 5H), 7.57 (s, 2H), 7.50 – 7.42 (m, 10H), 7.33 (dd, *J* = 16.0, 8.5 Hz, 4H), 2.12 (s, 3H), 1.39 (s, 36H). ^{13}C NMR (101 MHz, CD_2Cl_2) δ 153.26, 140.86, 136.15, 131.91, 131.03, 126.64, 126.16, 124.19, 123.70, 121.88, 121.45, 121.17, 120.74, 120.66, 120.34, 119.32, 113.13, 110.68, 108.37, 35.53, 31.64, 18.14. HRMS: *m/z* calculated for $C_{72}H_{69}N_4^+$: 989.5517 [*M*+H]$^+$, found: 989.5519.

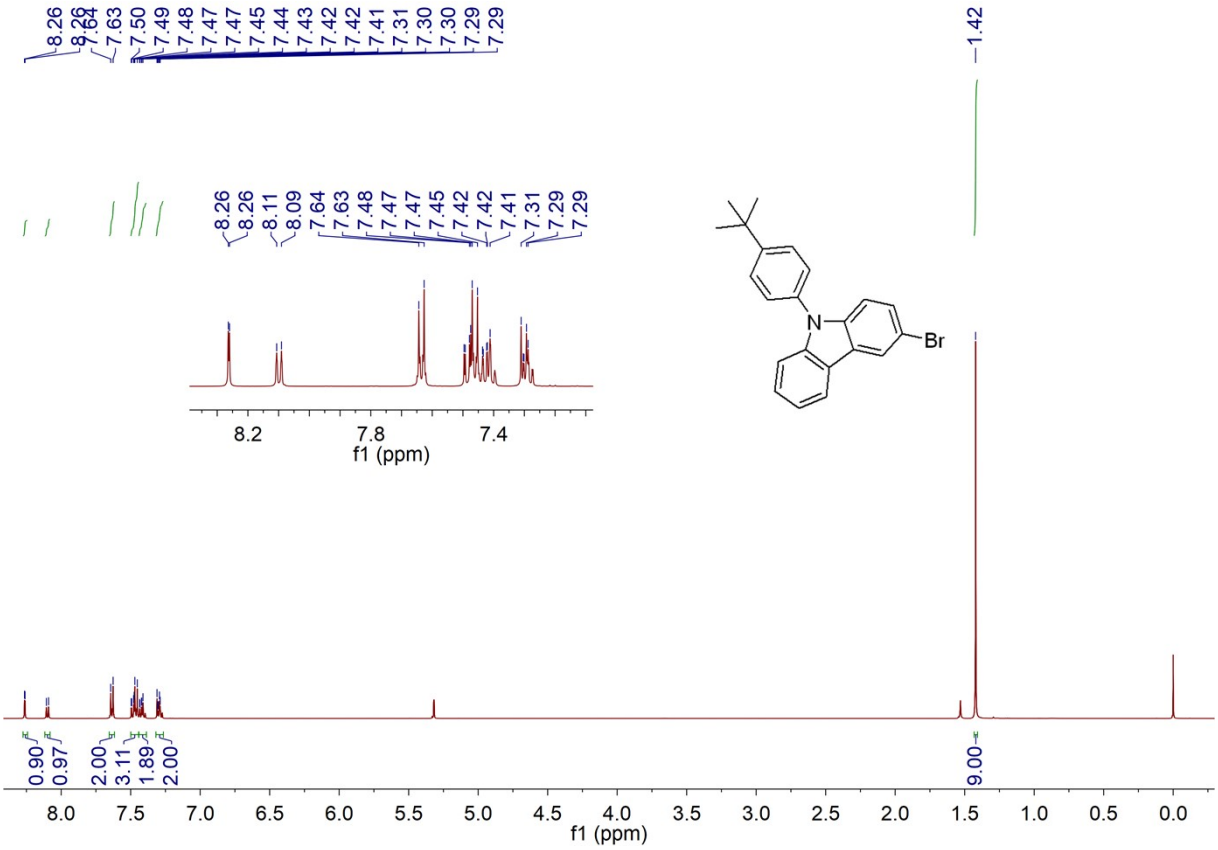

Figure S2. ^{1}H-NMR Spectrum of **2** ($C_{22}H_{20}BrN$) in CD_2Cl_2.

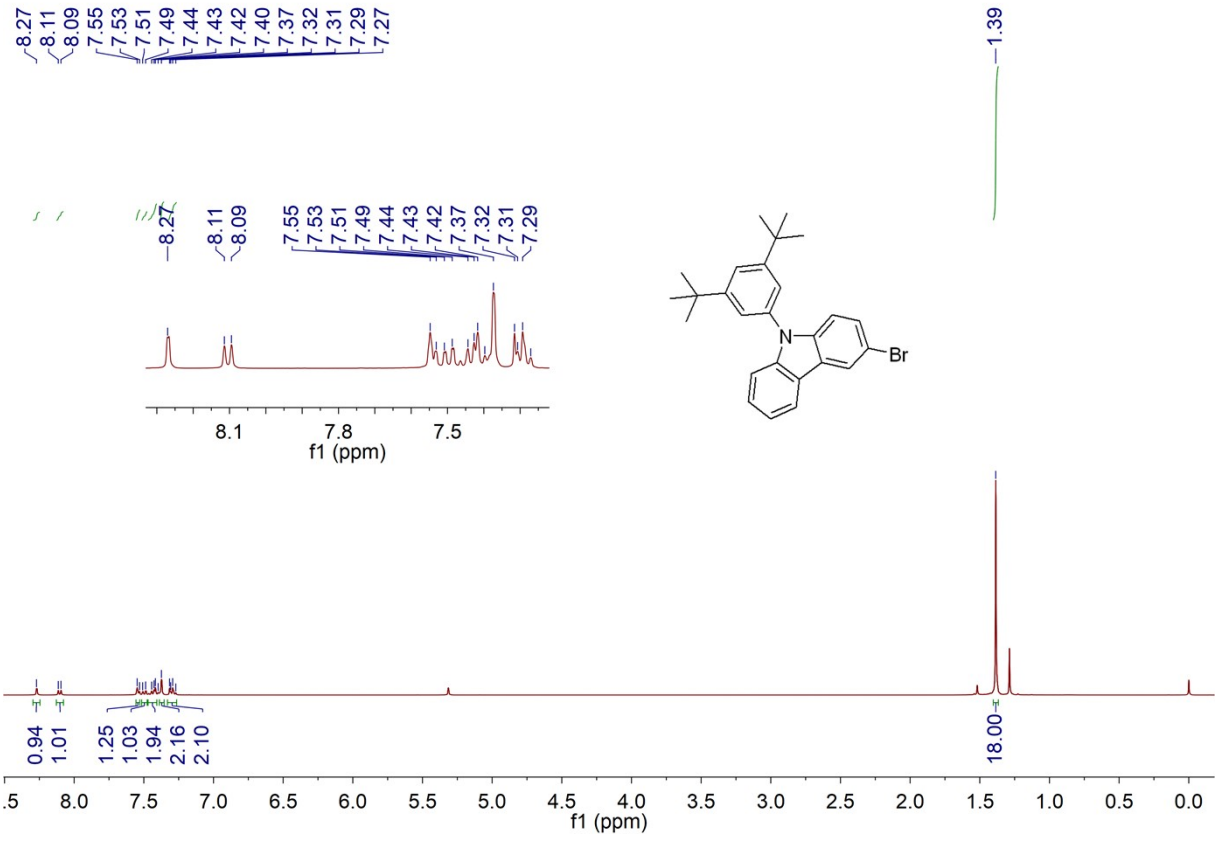

Figure S3. ^{1}H-NMR spectrum of **3** ($C_{26}H_{28}BrN$) in CD_2Cl_2.

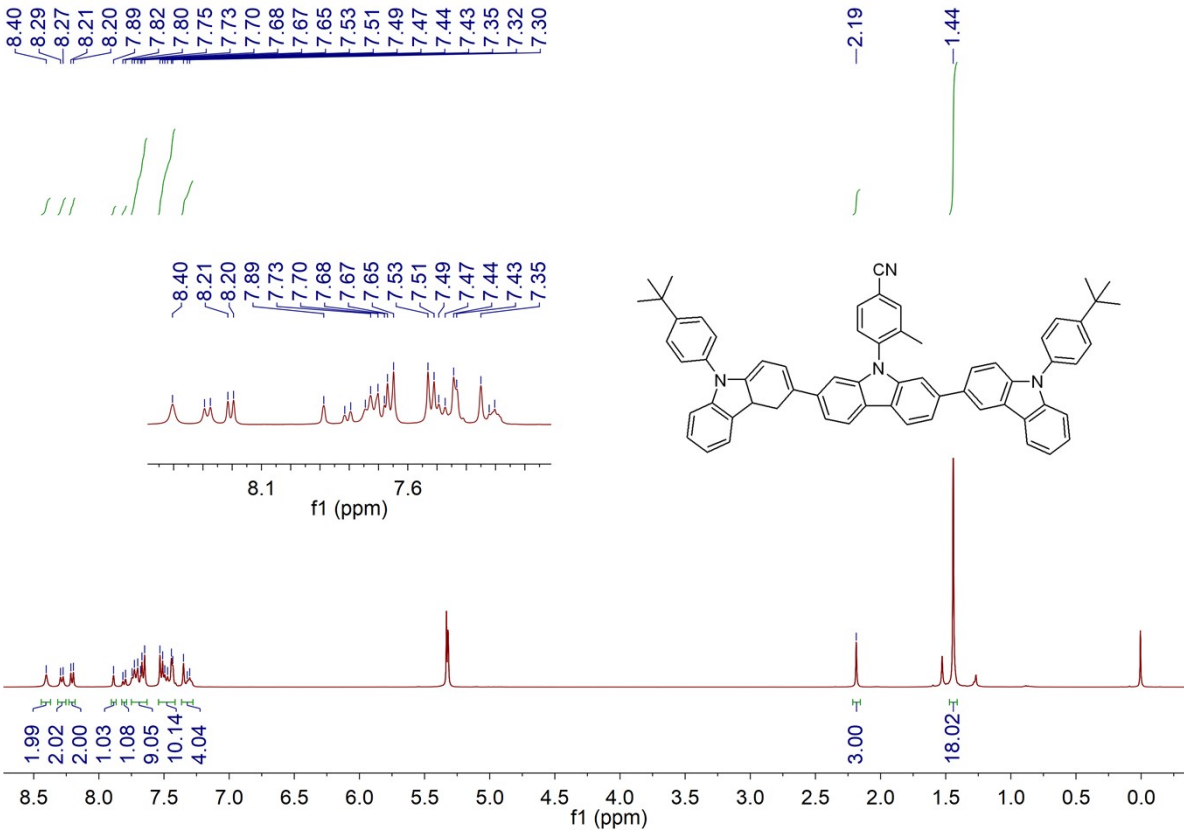

Figure S4. ^{1}H-NMR spectrum of **2*t*-2MCz-CNMCz** ($C_{64}H_{52}N_4$) in CD_2Cl_2.

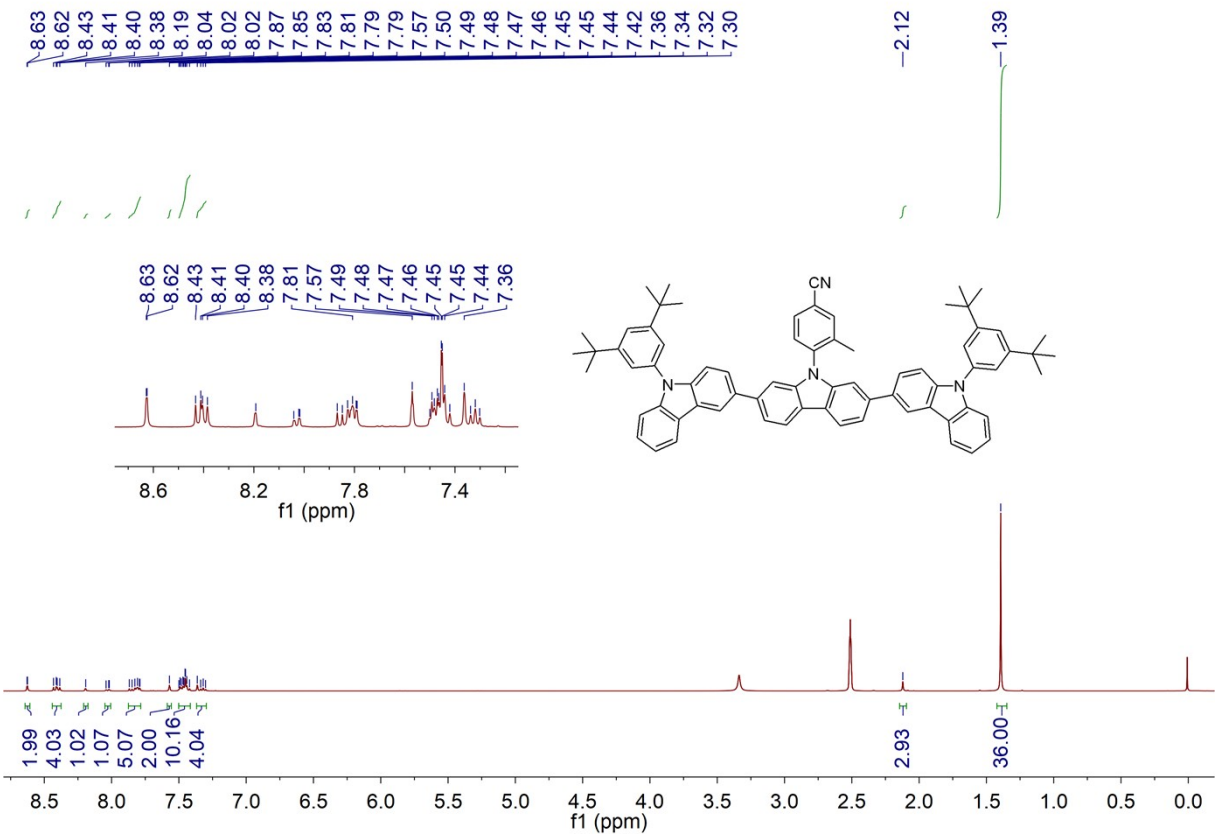

Figure S5. ^{1}H-NMR spectrum of **4*t*-2MCz-CNMCz** ($C_{72}H_{68}N_4$) in dimethyl sulfoxide-d6.

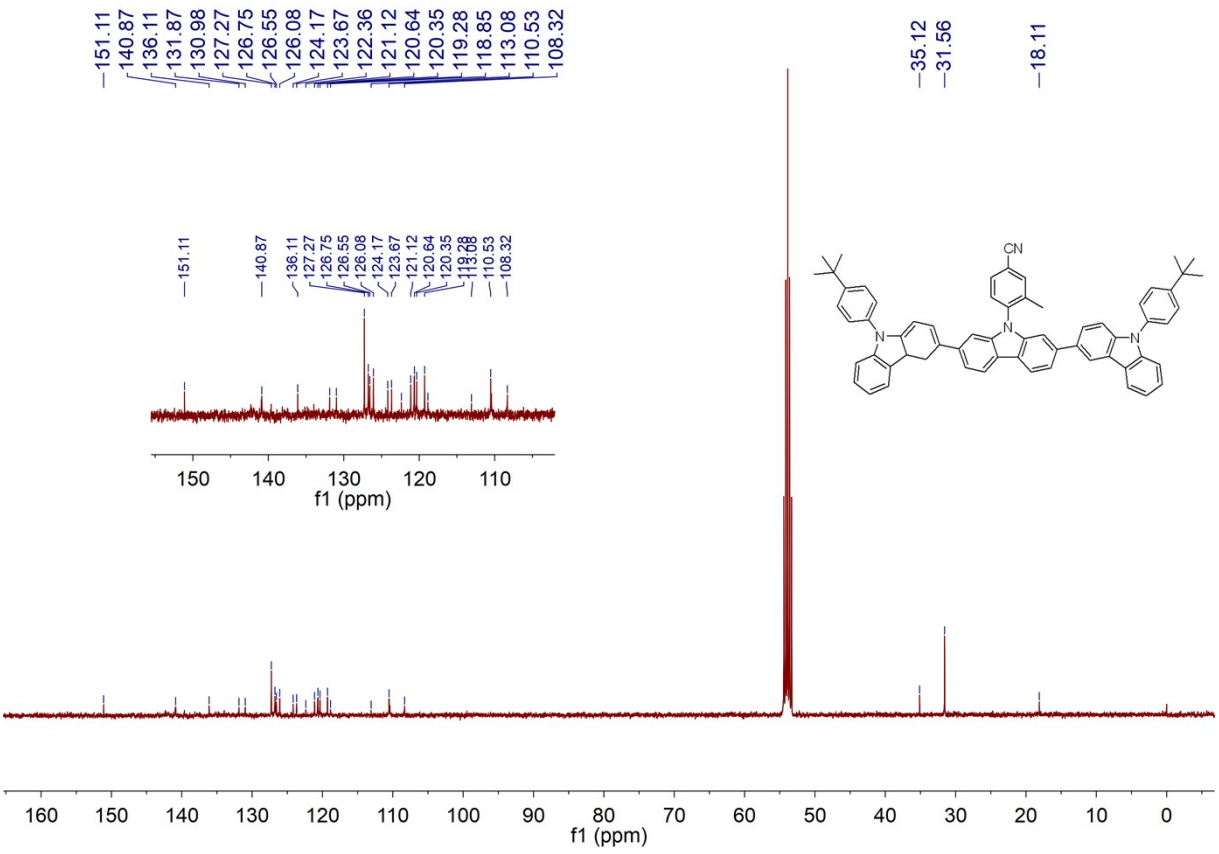

Figure S6. ^{13}C-NMR spectrum of **2*t*-2MCz-CNMCz** ($C_{64}H_{52}N_4$) in CD_2Cl_2.

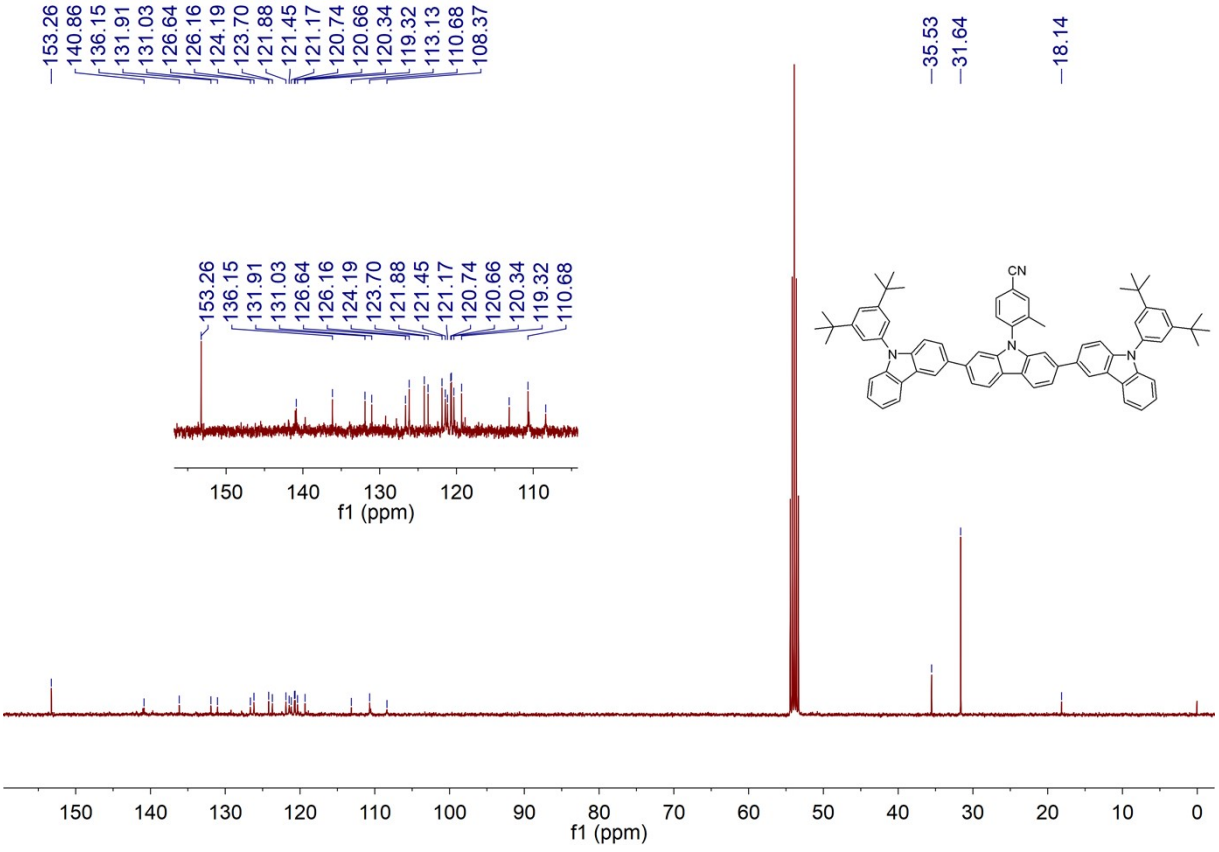

Figure S7. ^{13}C-NMR spectrum of **4*t*-2MCz-CNMCz** ($C_{72}H_{68}N_4$) in CD_2Cl_2.

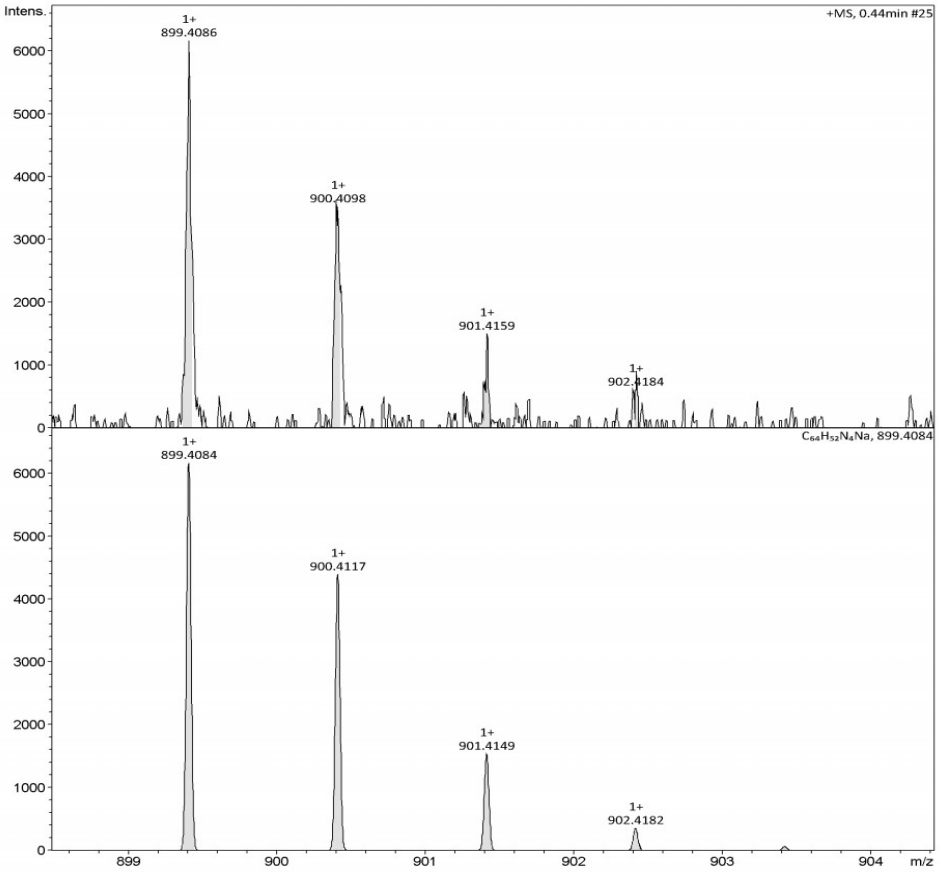

Figure S8. High resolution mass spectra (HRMS) of **2*t*-2MCz-CNMCz** ($C_{64}H_{52}N_4$)**.**

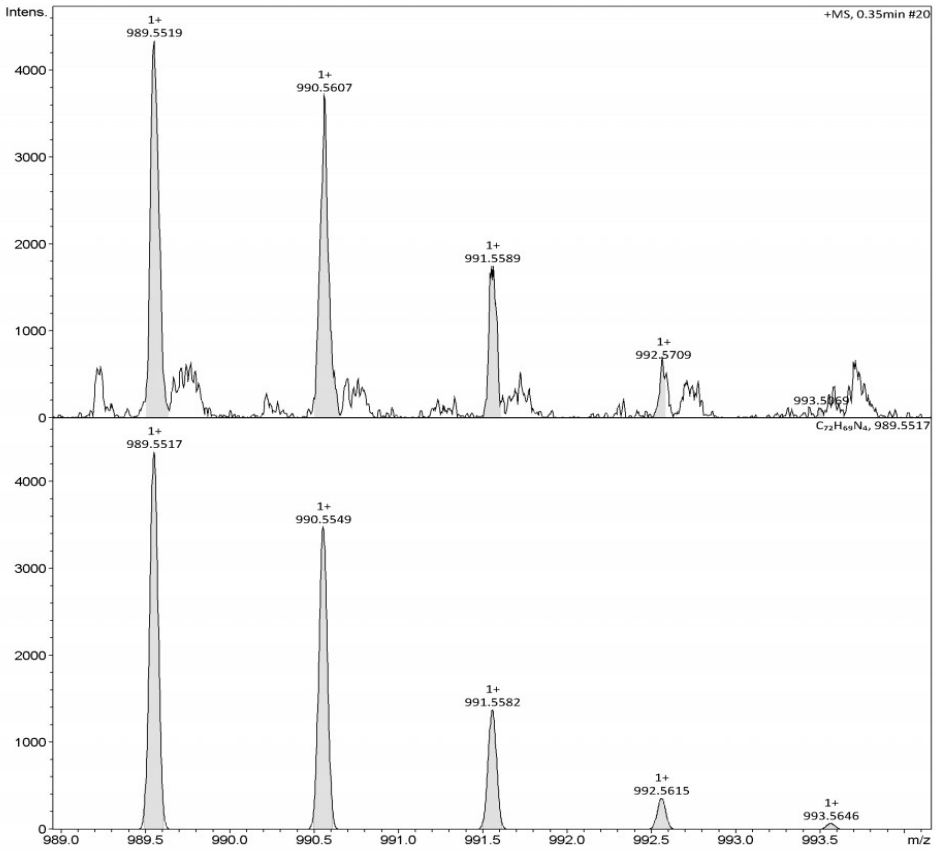

Figure S9. High resolution mass spectra (HRMS) of **4*t*-2MCz-CNMCz** ($C_{72}H_{68}N_4$)**.**

Table S2. Elemental analysis of 2*t*-2MCz-CNMCz and 4*t*-2MCz-CNMCz.

Compound	Chemical Formula	Weigh t /mg	Text ID	Experimental			Computational		
				N%	C%	H%	N%	C%	H%
2*t*-2MCz-CNMCz	$C_{64}H_{52}N_4$	1.115	136042-1	6.31	87.55	5.877	6.39	87.64	5.98
4*t*-2MCz-CNMCz	$C_{72}H_{68}N_4$	1.108	136042-2	5.47	87.08	6.579	5.66	87.41	6.93

Supporting figures and tables

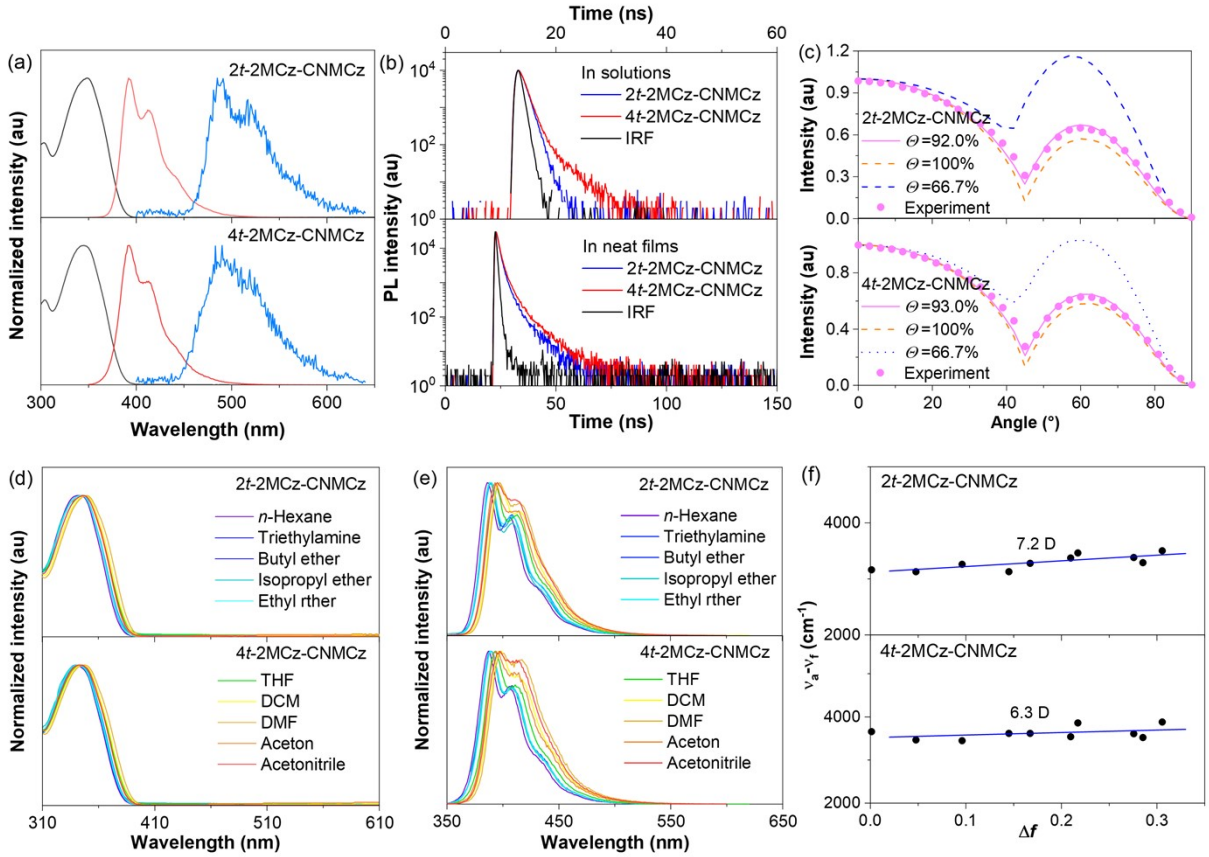

Figure S10. (a) UV-*vis* absorption (black), fluorescence spectra in 300 K (red), and phosphorescence spectra (blue) of 2*t*-2MCz-CNMCz and 4*t*-2MCz-CNMCz. (b) Transient PL decay curves in toluene solutions (top) and neat films (bottom). (c) *p*-Polarized angle-dependent PL radiance in neat films. (d) UV-vis absorptions in different solvents with various polarities. (e) UV-vis absorptions of 2*t*-2MCz-CNMCz and 4*t*-2MCz-CNMCz in different solvents with various polarities. (f) Solvatochromic *Lippert–Mataga* models of 2*t*-2MCz-CNMCz and 4*t*-2MCz-CNMCz.

Table S3. Optical, thermal, and electronic properties of 2*t*-2MCz-CNMCz and 4*t*-2MCz-CNMCz.

Compound	λ_{abs} [a] (nm)	λ_{em} (nm)		Φ_{PL} [c] (%)		τ [d] (ns)		$E_{S1}/E_{T1}/\Delta E_{S1T1}$ [e] (eV)	HOMO/ LUMO [f] (eV)
		soln [a]	film [b]	soln [a]	film [b]	soln [a]	film [b]		

2*t*-2MCz-CNMCz	349	392	406	85.3	60.3	1.1	1.2	3.29/2.68/0.61	2.24/5.53
4*t*-2MCz-CNMCz	345	393	425	93.2	55.6	1.2	2.2	3.32/2.77/0.55	2.24/5.54

[a]In toluene solution (10^{-5} M) at room temperature. [b]In neat film. [c]Absolute PLQY evaluated using a calibrated integrating sphere. [d]Fluorescence lifetime. [e]Estimated from the onsets of the fluorescence and phosphorescence spectra in toluene at 77 K. [f]HOMO and LUMO were measured from the oxidation potential by cyclic voltammetry with ferrocene as the external standard.

Table S4. Absorption and emission peak positions of 2*t*-2MCz-CNMCz in different solvents.

Solvents	ε[a]	n	$f(\varepsilon,n)$[b]	λ_a (nm)	λ_f (nm)	ν_a-ν_f (cm^{-1})[c]
n-Hexane	1.90	1.375	0.001	344	386	3163
Triethylamine	2.42	1.401	0.048	346	388	3129
Butyl ether	3.08	1.399	0.096	346	390	3261
Isopropyl ether	3.88	1.368	0.145	346	388	3129
Ethyl ether	4.34	1.352	0.167	345	389	3279
Tetrahydrofuran	7.58	1.407	0.210	347	393	3373
Dichloromethane	8.93	1.424	0.217	349	397	3464
Dimethyl formamide	37.00	1.427	0.276	350	397	3383
Acetone	20.70	1.359	0.284	348	393	3290
Acetonitrile	37.50	1.344	0.305	347	395	3502

[a]The solvent dielectric constant and *n* is the solvent refractive index. [b]The orientational polarizability of solvents. [c]The Stokes shift.

Table S5. Absorption and emission peak positions of 4*t*-2MCz-CNMCz in different solvents.

Solvents	ε[a]	n	$f(\varepsilon,n)$[b]	λ_a (nm)	λ_f (nm)	ν_a-ν_f (cm^{-1})[c]
n-Hexane	1.90	1.375	0.001	339	387	3659
Triethylamine	2.42	1.401	0.048	342	388	3467
Butyl ether	3.08	1.399	0.096	343	389	3448
Isopropyl ether	3.88	1.368	0.145	341	389	3619
Ethyl ether	4.34	1.352	0.167	341	389	3619
Tetrahydrofuran	7.58	1.407	0.210	345	393	3540
Dichloromethane	8.93	1.424	0.217	345	398	3860
Dimethyl formamide	37.00	1.427	0.276	348	398	3610
Acetone	20.70	1.359	0.284	346	394	3521
Acetonitrile	37.50	1.344	0.305	344	397	3881

[a]The solvent dielectric constant and *n* is the solvent refractive index. [b]The orientational polarizability of solvents. [c]The Stokes shift.

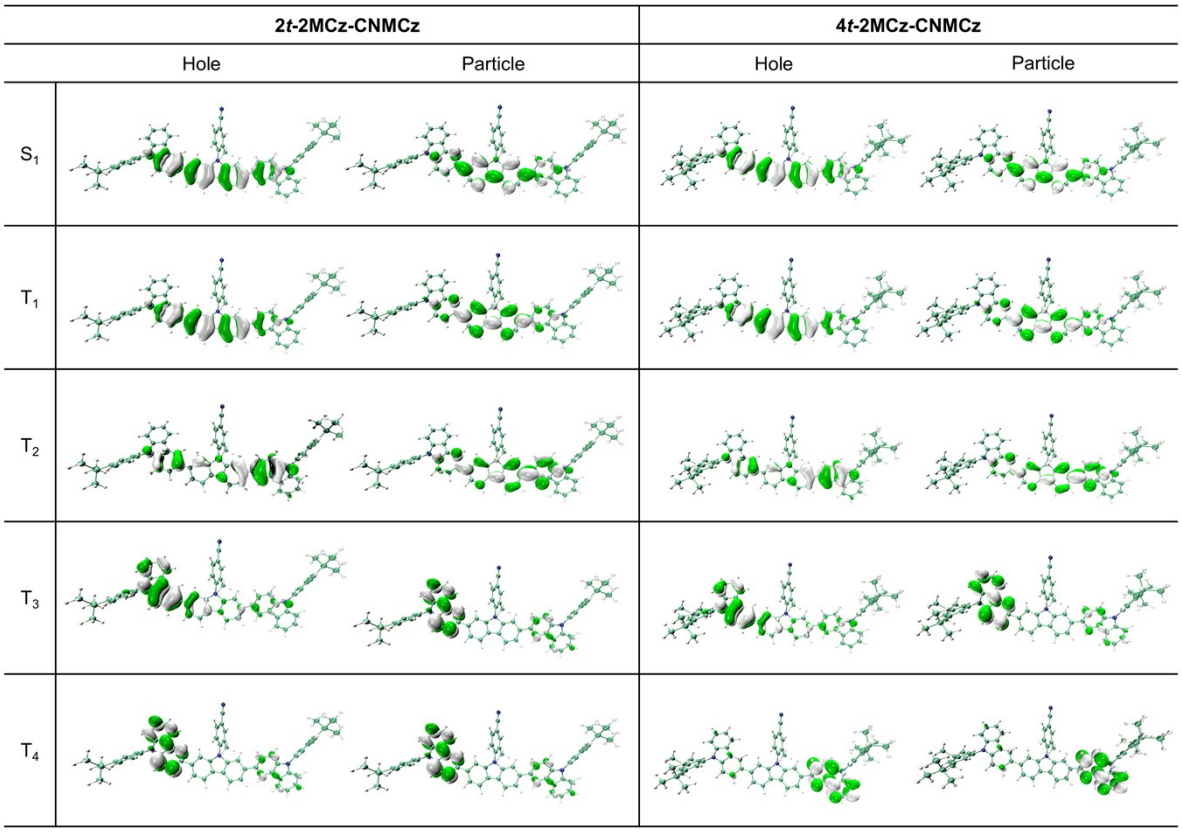

Figure S11. The frontier orbital distributions and NTOs distribution of 2*t*-2MCz-CNMCz and 4*t*-2MCz-CNMCz.

Table S6. Energy levels and SOC of singlet and triplet states of 2*t*-2MCz-CNMCz.

n=	1	2	3	4	5
S_n /eV	3.226	3.874	3.887	3.964	3.997
T_n /eV	2.461	3.174	3.416	3.428	3.459
($\langle S_1\hat{H}SOT_n\rangle$) /cm^{-1}	0.033	0.224	0.072	0.173	0.117

Table S7. Energy levels and SOC of singlet and triplet states of 4*t*-2MCz-CNMCz.

n=	1	2	3	4	5
S_n /eV	3.223	3.870	3.886	3.960	3.994
T_n /eV	2.461	3.170	3.413	3.425	3.459
($\langle S_1\hat{H}SOT_n\rangle$) /cm^{-1}	0.033	0.206	0.081	0.191	0.117

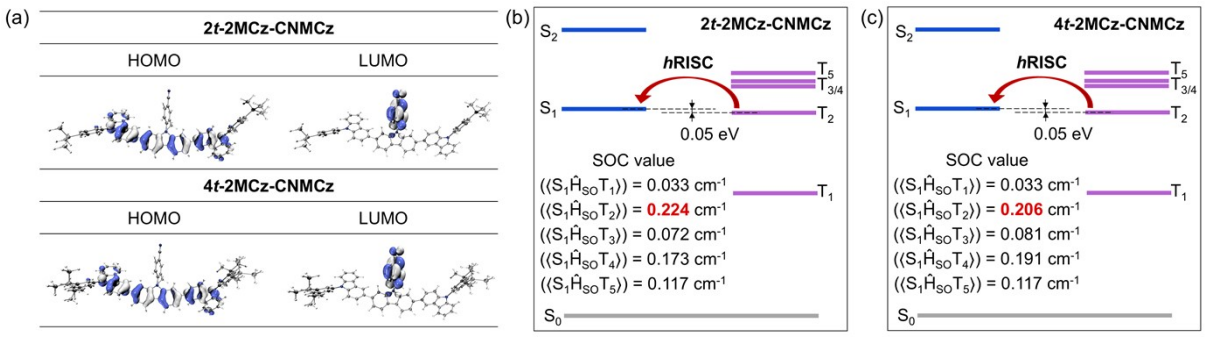

Figure S12. The HOMO, LUMO distribution, and proposed hot-exciton mechanisms of 2*t*-2MCz-CNMCz and 4*t*-2MCz-CNMCz. The S_1 energy level of 2*t*-2MCz-CNMCz and 4*t*-2MCz-CNMCz was calculated to be 3.23 eV to 3.22 eV, and the T_1 energy levels are also calculated to be 2.46 eV and 2.46 eV. It can be noted that the energy gaps (ΔE_{ST}) between the high-lying triplet states (T_2, T_3, and T_4) and S_1 states are relatively small for both 2*t*-2MCz-CNMCz and 4*t*-2MCz-CNMCz. This kind of energy-level distribution could facilitate the triplet-to-singlet conversion through the hot-exciton channels. The NTO distribution of T_2 level exhibits the hybrid local and charge-transfer feature. In addition, for both 2*t*-2MCz-CNMCz and 4*t*-2MCz-CNMCz, the spin-orbital coupling (SOC) values between S_1 and T_2 ($\langle S_1\hat{H}SOT_2\rangle$) are remarkably larger than $\langle S_1\hat{H}SOT_3\rangle$ and $\langle S_1\hat{H}SOT_4\rangle$, which implies that $T_2 \rightarrow S_1$ might be dominant in the hot-exciton channels.

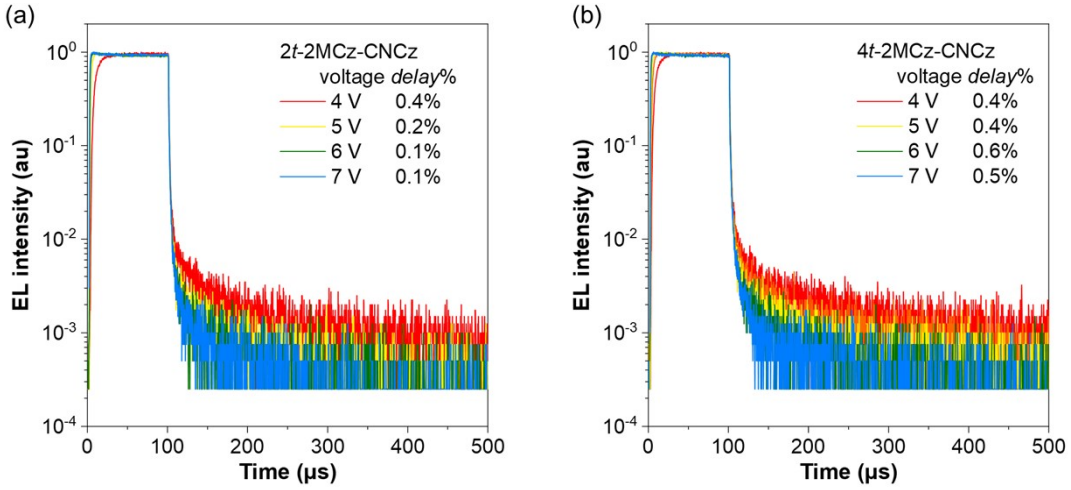

Figure S13. The transient EL curves of the (a) 2*t*-2MCz-CNMCz and (b) 4*t*-2MCz-CNMCz (insert: the TTA contribution is defined as the ratio of delayed emission to total emission (*delay*%)).

The transient electroluminescence (EL) curves of the 2*t*-2MCz-CNMCz and 4*t*-2MCz-CNMCz were provided. The transient EL curves of 2*t*-2MCz-CNMCz and 4*t*-2MCz-CNMCz were fitted by equation:

$$y = \frac{1}{(At + B)^2}$$

where y is the EL intensity under constant voltage, t is the time, A and B represent the fitting constant. It was found that the two molecules exhibited markedly small *delay*% values at different voltages. The maximum *delay*% of 2*t*-2MCz-CNMCz and 4*t*-2MCz-CNMCz were 0.4% and 0.6%, respectively, indicating that the triplet excitons of 2*t*-2MCz-CNMCz and 4*t*-2MCz-CNMCz were harvested through processes other than the triplet-triplet annihilation (TTA) mechanism.

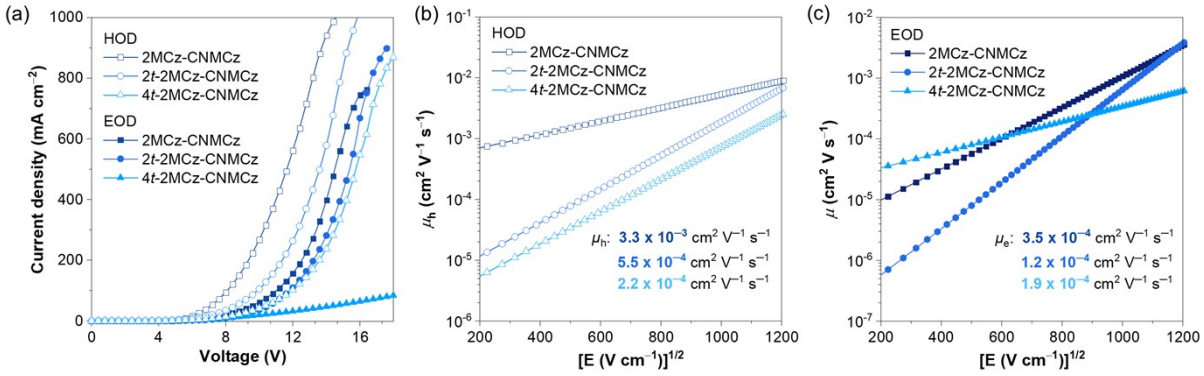

Figure S14. (a) Current density-voltage and carrier mobilities (μ_h for hole and μ_e for electron)-electric field curves of (b) hole-only devices (HODs) and (c) electron-only (EODs) of hot-exciton materials. The EODs and HODs were fabricated with the configuration of ITO/TmPyPB (10 nm)/EML (80 nm)/TmPyPB (10 nm)/LiF (1 nm)/Al (120 nm), and ITO/TAPC (10 nm)/EML (80 nm)/TAPC (10 nm)/Al (120 nm), in which the EML is 2MCz-CNMCz, 2*t*-2MCz-CNMCz, and 4*t*-2MCz-CNMCz, respectively.

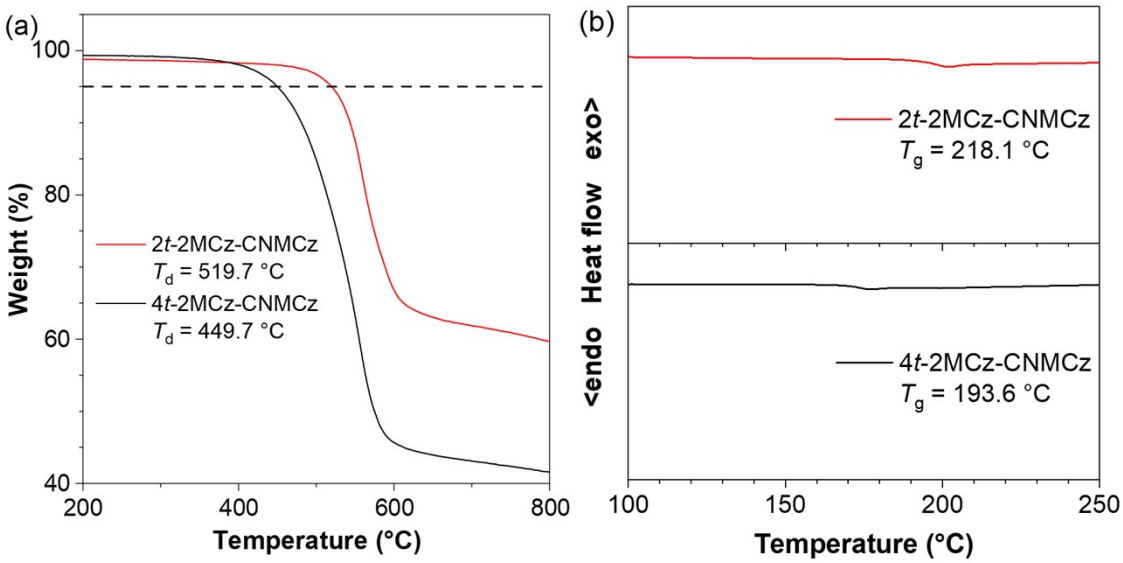

Figure S15. (a) Thermogravimetric analysis curves. (b) Differential scanning calorimetry curves.

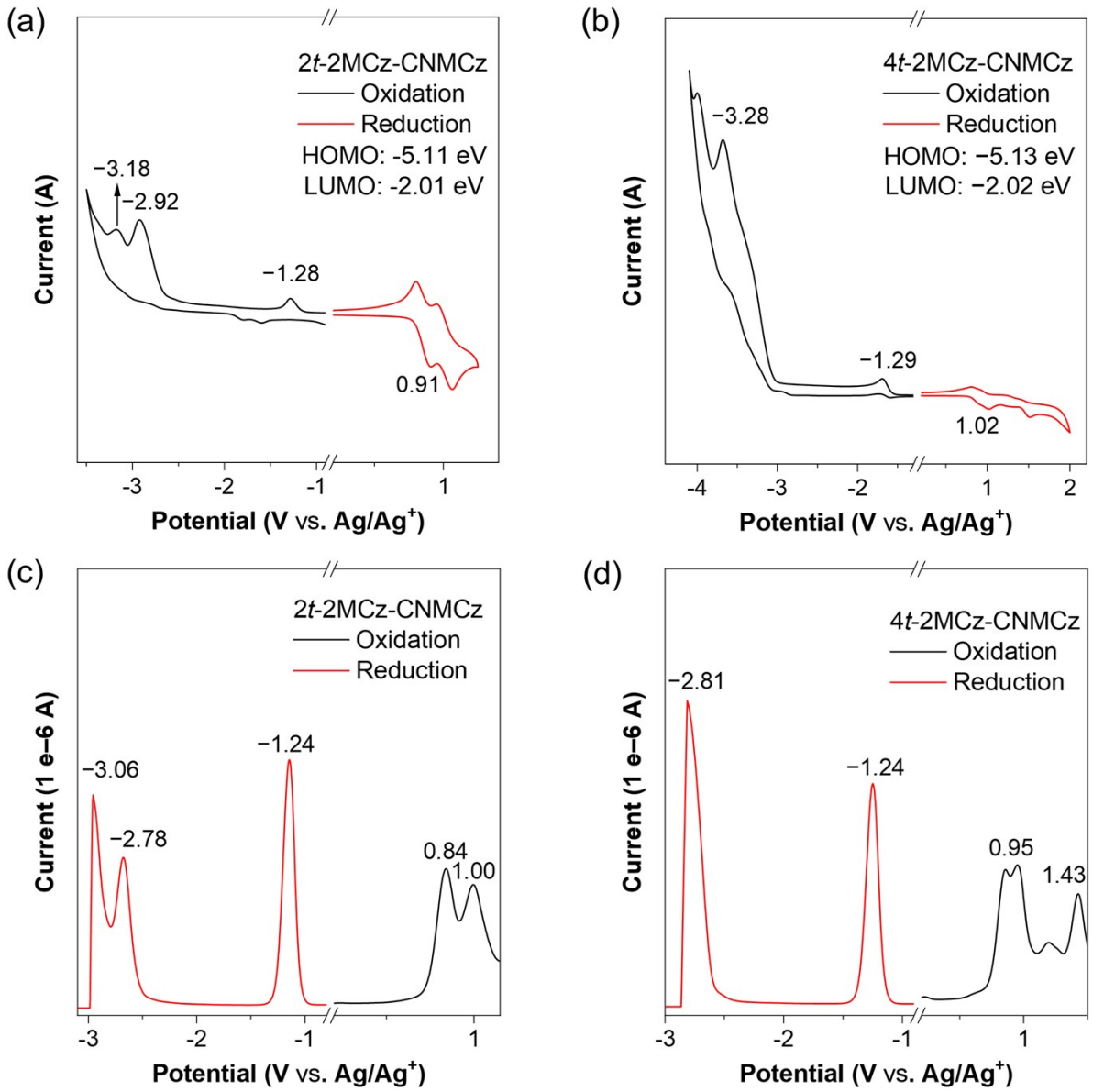

Figure S16. Cyclic voltammograms of (a) 2*t*-2MCz-CNMCz and (b) 4*t*-2MCz-CNMCz, measured in DCM/DMF containing 0.1 m tetra-*n*-butylammonium hexafluorophosphate. Differential pulse voltammetry data (c) 2*t*-2MCz-CNMCz and (d) 4*t*-2MCz-CNMCz.

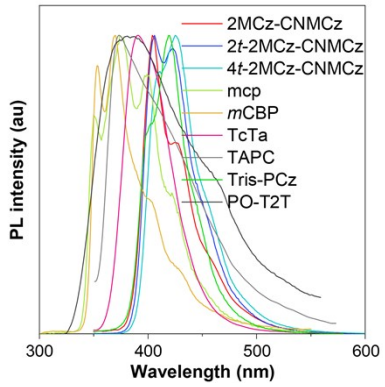

Figure S17. PL spectra of donor and acceptor.

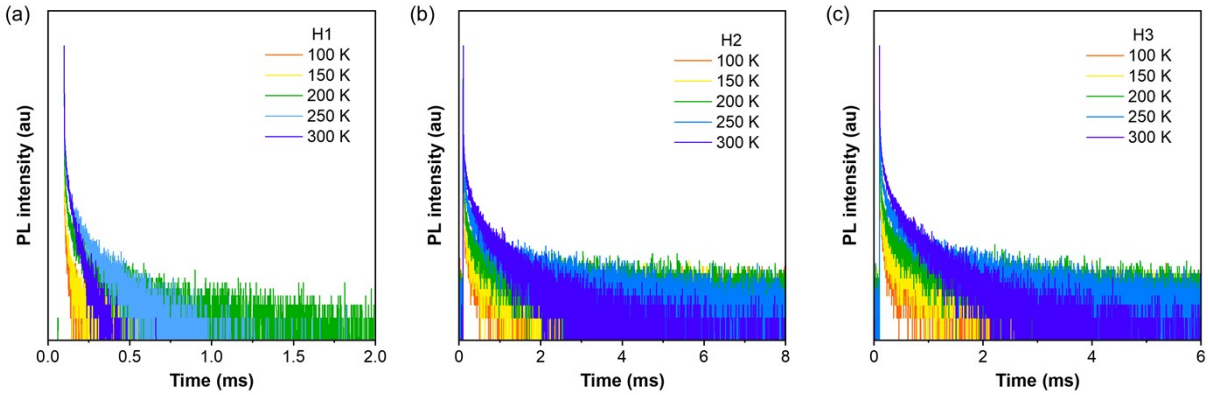

Figure S18. Temperature-dependent transient PL decay spectra of the films of exciplex H1, H2, and H3, respectively.

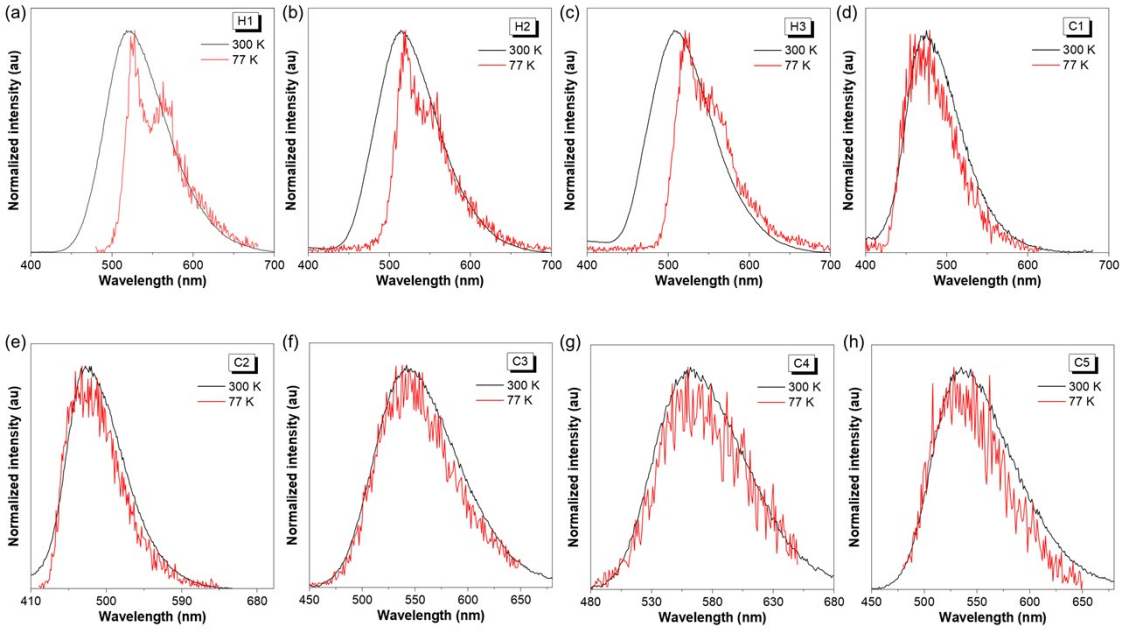

Figure S19. Fluorescence spectra (black line) at 300 K and phosphorescence spectra (red line) at 77 K of different exciplex films.

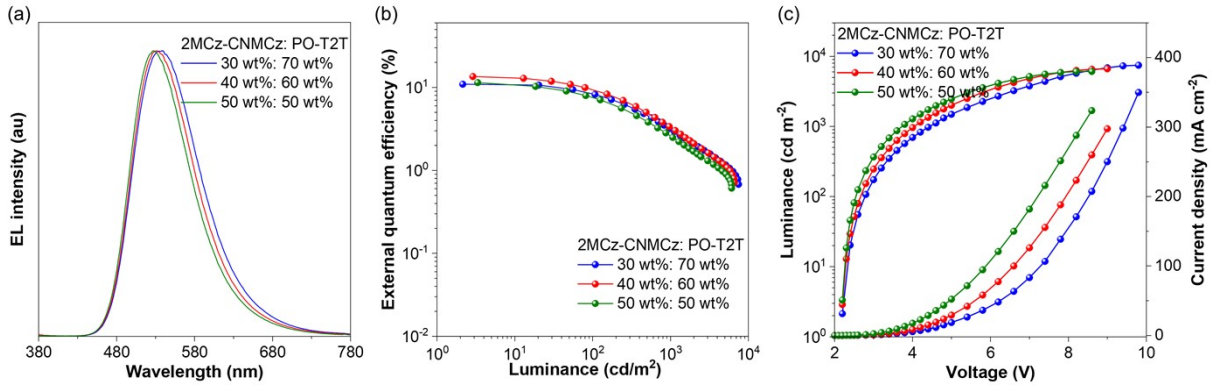

Figure S20. (a) EL spectrum of the devices at 10 mA cm^{-2}. (b) EQE–luminance characteristics. (c) Current density and luminance versus voltage (*J*-*V*-*L*) characteristics of devices (insert: the weight fraction of 2MCz-CN-MCz and PO-T2T, respectively). The exciplex-based OLEDs

with varying donor-acceptor weight ratios were fabricated, and it demonstrated that the device attained optimal external quantum efficiency and power efficiency when the donor and acceptor were formulated at 40 wt% and 60 wt%, respectively.

Table S8. Electroluminescence performances of devices with different concentrations.

2MCz-CN-MCz: PO-T2T	λ_{EL} (nm)	V_{on} [a] (V)	L [b] (cd m^{-2})	CE_{max} [c] (cd A^{-1})	PE_{max} [d] (lm W^{-1})	$EQE_{max/100}$ [e] (%)	CIE (x, y)[f]
30 wt%: 70 wt%	538	2.2	7465	35.6	50.8	10.9/8.2	0.358, 0.569
40 wt%: 60 wt%	532	2.2	6632	45.3	64.7	13.5/10.0	0.341, 0.576
50 wt%: 50 wt%	528	2.2	6095	38.1	54.4	11.5/8.0	0.326, 0.579

[a]Turn-on voltage ≥ 1 cd m^{-2}. [b]Maximum luminance. [c]Maximum current efficiency. [d]Maximum PE. [e]Maximum EQE/EQE at 100 cd m^{-2}. [f]Commission internationale de l'éclairage, recorded at 10 mA cm^{-2}.

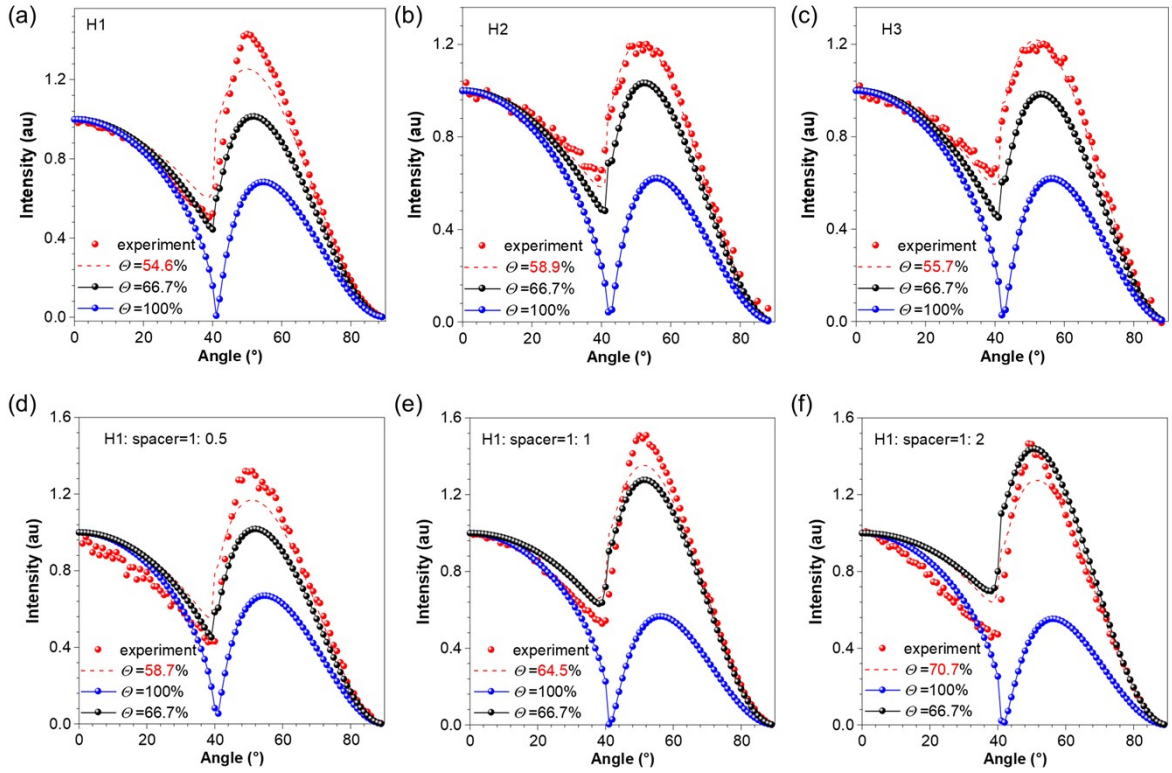

Figure S21. Variable-angle PL measurement of films of three HE-type exciplexes and the exciplexes doping DPEPO of different ratios. *Θ* was orientation factor. For fully horizontal dipoles, *Θ* equals 100% and isotropic dipole orientation, *Θ* equals 67%. The refractive indices of the functional materials and the emitters were measured on J. A. Woolam V-VASE spectroscopic ellipsometer with a wavelength range of 300-1000 nm. The step size was 10 nm, and the incident angle was 75°. The material neat films were prepared by evaporating on crystalline silicon and the thickness of each material films were 30 nm. In this work, the refractive indices of HATCN, TAPC, TcTa, exciplex, PO-T2T at were measured as 1.57±0.1,

1.75±0.1, 1.53±0.1, 1.79±0.1 (H1), 1.74±0.1 (H1: DPEPO=1: 0.5), 1.72±0.1 (H1: DPEPO=1: 1), and 1.69±0.1 (H1: DPEPO=1: 2) green emission. The OLED model was constructed by Ansys Lumerical FDTD, and the vertical optical outcoupling efficiencies ($\eta_{\perp}$) were evaluated to 0.55%, 0.55%, 0.57%, and 0.56%, and the horizontal optical outcoupling efficiencies ($\eta_{\parallel}$) were evaluated to 46.8%, 46.8%, 47.4%, and 48.2%. Based on the horizontal transition dipole ratios ($\Theta_{//}$), the optical outcoupling efficiencies (η_{out}) were calculated to be 25.8%, 27.7%, 30.8%, and 34.3%, respectively.

Table S9. Optical coupling output efficiencies of OLEDs with doping H1 into DPEPO host.

Device	percentage by weight of H1 and spacer	optical coupling output efficiency [%]
D0	1: 0.5	27.7
D1	1: 1	30.8
D2	1: 2	34.3

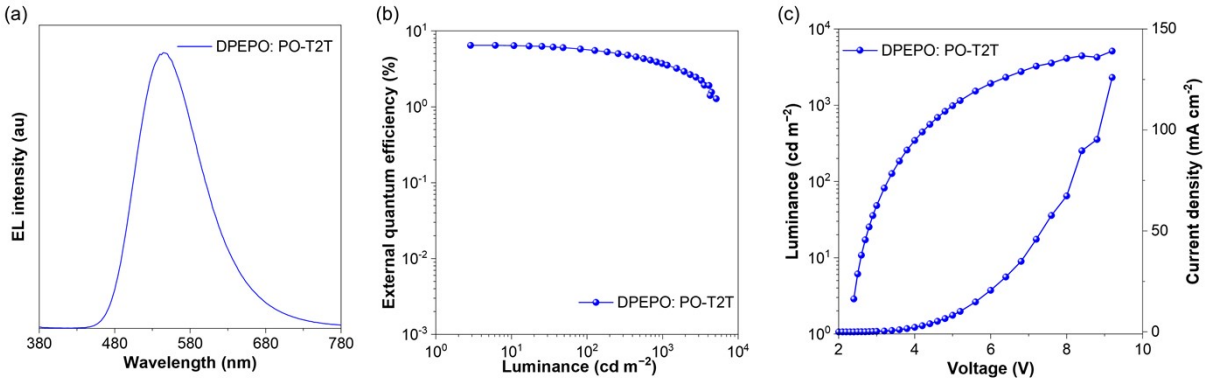

Figure S22. a EL spectrum of the devices at 10 mA cm^{-2}. **b** EQE–luminance characteristics. **c** Current density and luminance versus voltage (*J-V-L*) characteristics of devices. The DPEPO could form exciplex with PO-T2T under electroluminescence, however, the device based on exciplex (40 wt% DPEPO and 60 wt% PO-T2T) exhibited an emission wavelength of 544 nm, which was obviously different with the emission of device D1 (526 nm). The device exhibited a maximum EQE of 6.5% and a PE of 26.2 lm W^{-1}, indicating the maximum EQE of 19.0% and PE of 82.1 lm W^{-1} of device D1 was not contributed by DPEPO.

Table S10. Electroluminescence performance.

DPEPO: PO-T2T	λ_{EL} (nm)	V_{on} [a] (V)	L [b] (cd m^{-2})	CE_{max} [c] (cd A^{-1})	PE_{max} [d] (lm W^{-1})	$EQE_{max/1000}$ [e] (%)	CIE (x, y)[f]
40 wt%: 60 wt%	544	2.4	5122	20.3	26.2	6.5/3.5	0.385, 0.559

[a]Turn-on voltage ≥ 1 cd m^{-2}. [b]Maximum luminance. [c]Maximum current efficiency. [d]Maximum PE. [e]Maximum EQE/EQE at 1000 cd m^{-2}. [f]Commission internationale de l'éclairage, recorded at 10 mA cm^{-2}.

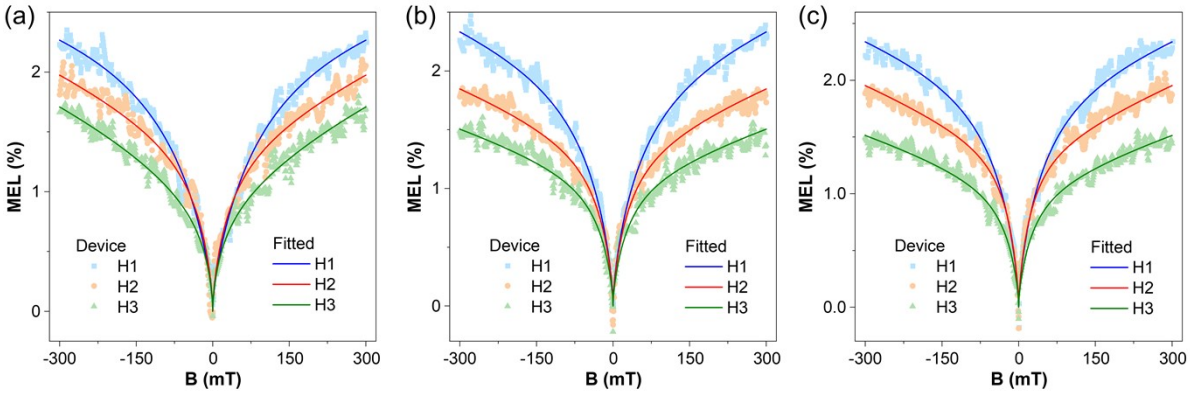

Figure S23. The MEL responses of devices H1, H2, and H3 at different current densities of (a) 10 mA cm^{-2}, (b) 15 mA cm^{-2}, and (c) 20 mA cm^{-2}, respectively.

The Δg factor model:

$$MEL = A\frac{B}{(|B| + B_0)^2} + C \cdot \sqrt{|B|}$$

in which *MEL* is the change of EL intensity as the magnetic field strength changed under constant current, B is the magnetic field strength, A and B_0 represent the fitting constant and linewidth at low magnetic field (0-50 mT), respectively, and C is the fitting constant at high magnetic field.

Table S11. The values of C of devices H1, H2, and H3 at different current densities.

Device	5 mA cm^{-2}	10 mA cm^{-2}	15 mA cm^{-2}	20 mA cm^{-2}
H1	0.135	0.086	0.103	0.102
H2	0.122	0.099	0.089	0.095
H3	0.100	0.093	0.073	0.074

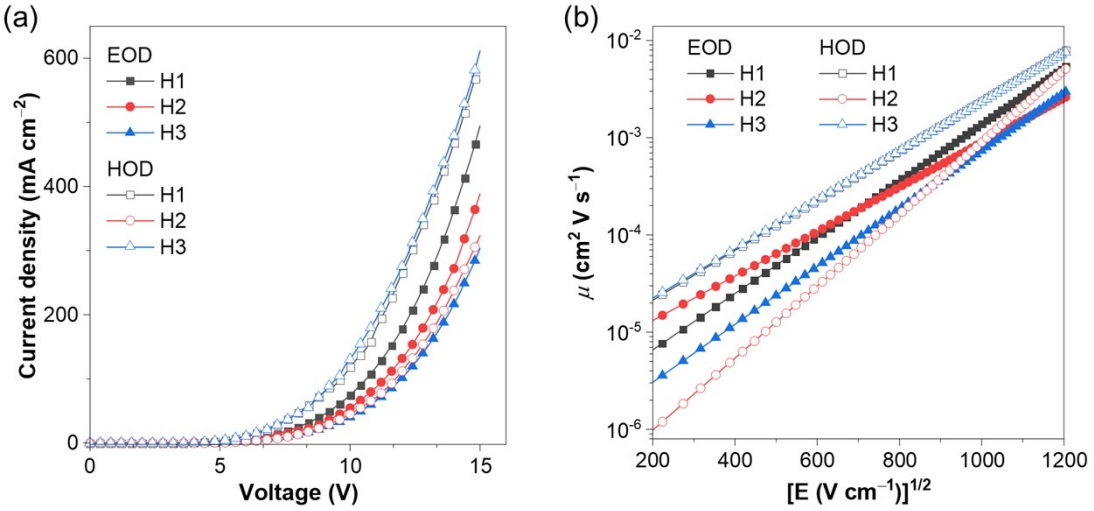

Figure S24. (a) Current density-voltage and (b) carrier mobilities (μ)-electric field curves of H-type exciplexes. The EODs and HODs were fabricated with the configuration of ITO/TmPyPB

(10 nm)/EML (80 nm)/TmPyPB (10 nm)/LiF (1 nm)/Al (120 nm), and ITO/TAPC (10 nm)/EML (80 nm)/TAPC (10 nm)/Al (120 nm), in which the EML is H1, H2, and H3, respectively. Compared to the exciplex H1, the electron mobility of H2 decreased, and both the electron and hole mobilities of H3 decreased, resulting in a decrease in efficiencies.

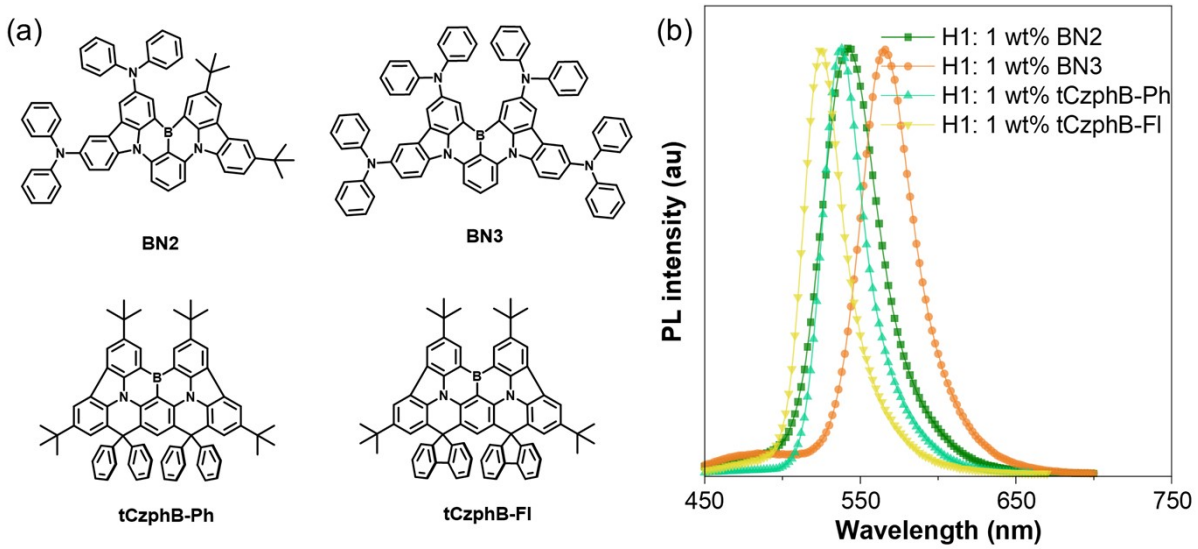

Figure S25. The chemical structures of four MR-TADF emitters and the PL spectra of sensitized films.

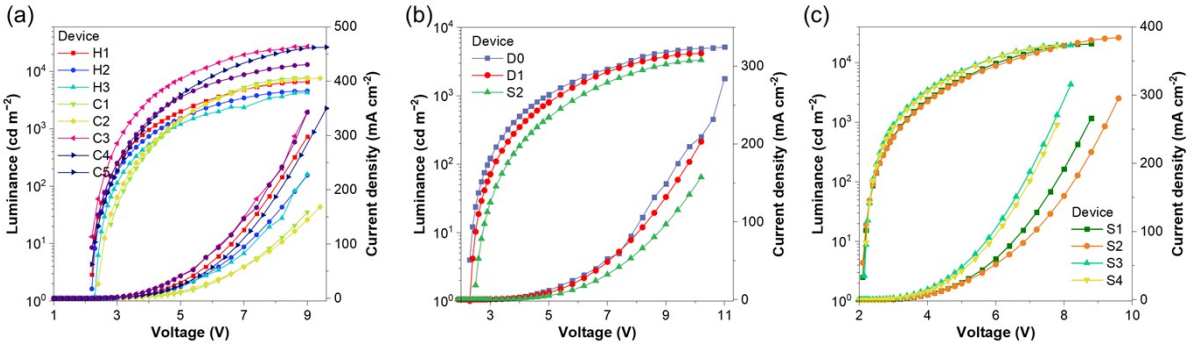

Figure S26. The current density and luminance versus voltage (*J-V-L*) characteristics of every OLEDs.

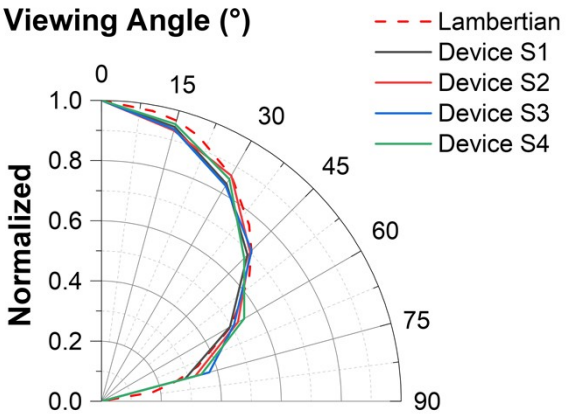

Figure S27. The angle-dependent EL intensities of the devices S1~S4. The correction factor of the devices S1~S4 were 0.97, 1.02, 1.02, 1.02 and the resulting corrected EQE were 36.5%, 41.1%, 31.4%, and 34.2%, respectively. The correction factors were close to 1, proving that the devices S1~S4 were close to *Lambertian* emission.

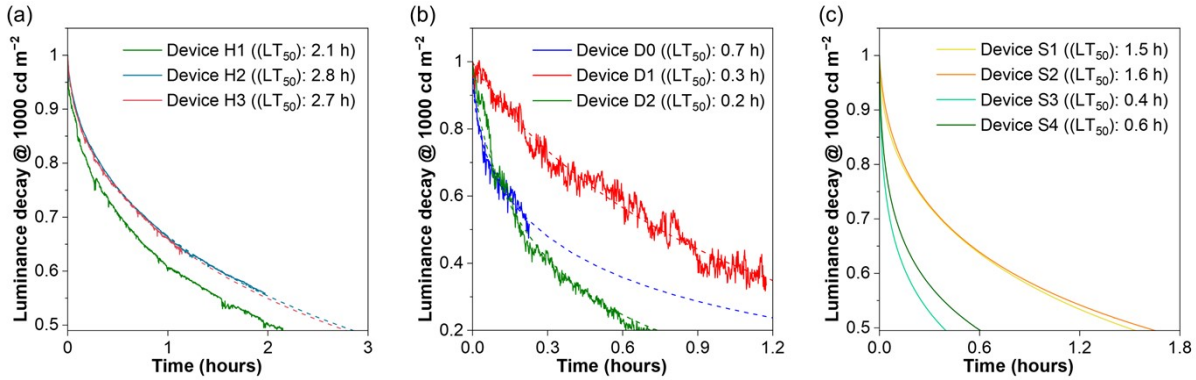

Figure S28. The luminance decay at 1000 cd m^{-2} of all hot-exciton materials-based devices.

The operational stabilities of a series of hot-exciton materials-based devices were evaluated, in which the luminance decay curves of devices H2, H3, D0, D1, D2 were further fitted by equation:

$$L = L_0 exp(-(t/\tau)^{\beta})$$

where L_0 is the initial luminance, t is the time, τ and β represent the fitting constants. It was found that the fitted curves completely cover experimental data. As a result, the operational lifetime to 50% (LT_{50}) of devices H1~H3 at an initial luminance of 1000 cd m^{-2} were 2.1, 2.8, and 2.7 h, respectively. The LT_{50} of devices D0~D2 at an initial luminance of 1000 cd m^{-2} were reduced to 0.7, 0.3, and 0.2 h. The LT_{50} of devices S1~S4 at an initial luminance of 1000 cd m^{-2} were 1.5, 1.6, 0.4 and 0.6 h, respectively.

Table S12. EQE_{max}-λ_{max} summary data of OLEDs with high PE.

λ_{max} (nm)	EQE_{max} (%)	PE_{max} (lm W^{-1})	Reference
544	37.7	232.8	**this work**
568	40.5	223.5	**this work**
526	30.7	176.6	**this work**
534	33.4	203.6	**this work**
536	34.4	166.3	Ref.3
532	36.1	187.7	Ref.4
558	40.5	205.8	Ref.5
560	38.7	170.7	Ref.5
540	37.6	136.8	Ref.6
540	41.9	197.3	Ref.7

References

[1] S. Zeng, Y. Xie, W. Huang, C. Wei, Y. Deng, P. Zou, C. Li, T.-T. Chen, Z. Zhao, Z. He, *Angew. Chem. Int. Ed.* **2025**, e24293

[2] X. Guo, G. Li, J. Lou, K. Chen, R. Huang, D. Yang, H. Zhang, Z. Wang, B. Z. Tang, *Small*, 2022, **18**, 2204029

[3] X. Wu, X. Peng, L. Chen, B. Z. Tang and Z. Zhao, *ACS Mater. Lett.*, 2023, **5**, 664.

[4] C. Yin, Y. Xin, T. Huang, Q. Zhang, L. Duan and D. Zhang, *Nat. Commun.*, 2025, **16**, 30.

[5] Y. X. Hu, J. Miao, T. Hua, Z. Huang, Y. Qi, Y. Zou, Y. Qiu, H. Xia, H. Liu, X. Cao and C. Yang, *Nat. Photon.*, 2022, **16**, 803−810.

[6] Y. Fu, H. Liu, B. Z. Tang and Z. Zhao, *Nat. Commun.*, 2023, **14**, 2019.

[7] J. Zeng, S. Song, Y. Fu, X. Peng, B. Z. Tang and Z. Zhao, *Sci. Adv.*, 2025, **11**, eadt7899.